Article

Anionic Disorder and Its Impact on the Surface Electronic Structure of Oxynitride Photoactive Semiconductors

Anna Hartl, Ján Minár, Procopios Constantinou, Vladimir Roddatis, Fatima Alarab, Arnold M. Müller, Christof Vockenhuber, Thorsten Schmitt, Daniele Pergolesi, Thomas Lippert, Vladimir N. Strocov,* and Nick A. Shepelin*

Read Online

ACCESS | Metrics & More | Article Recommendations | SI Supporting Information

ABSTRACT: The conversion of solar energy into chemical energy, stored in the form of hydrogen, bears enormous potential as a sustainable fuel for powering emerging technologies. Photoactive oxynitrides are promising materials for splitting water into molecular oxygen and hydrogen. However, one of the issues limiting widespread commercial use of oxynitrides is degradation during operation. While recent studies have shown the loss of nitrogen, its relation to reduced efficiency has not been directly and systematically addressed with experiments. In this study, we demonstrate the impact of the anionic stoichiometry of $BaTaO_xN_y$ on its electronic structure and functional properties. Through experimental ion scattering, electron microscopy, and photoelectron spectroscopy investigations, we determine the anionic composition ranging from the bulk toward the surface of $BaTaO_xN_y$ thin films. This further serves as input for band structure computations modeling the substitutional disorder of the anion sites. Combining our experimental and computational approaches, we reveal the depth-dependent elemental composition of oxynitride films, resulting in downward band bending and the loss of semiconducting character toward the surface. Extending beyond idealized systems, we demonstrate the relation between the electronic properties of real oxynitride photoanodes and their performance, providing guidelines for engineering highly efficient photoelectrodes and photocatalysts for clean hydrogen production.
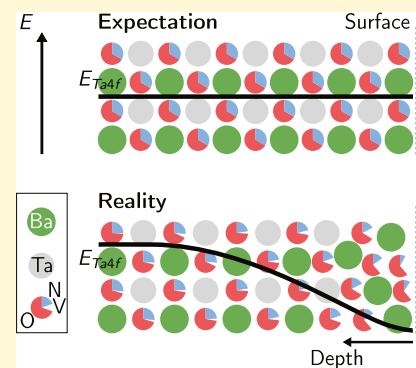
INTRODUCTION

Solar-driven water splitting converts light into chemical energy, which is consequently stored in the form of O_2 and H_2.[1] This sustainable generation of clean hydrogen fuel bears significant potential for nonfossil energy production in the future.[2−4] However, the efficiency of the involved photoactive materials must be improved for large-scale use. Indeed, the main challenge in the water splitting process is the production of molecular oxygen as part of the so-called oxygen evolution reaction (OER), whereby the efficiency is often hindered by high overpotentials and ill-defined reaction kinetics.[5] During the past two decades, research in the fields of photocatalysis and photoelectrochemistry (PEC) has explored oxynitride materials that have demonstrated notable suitability for water splitting applications.[6,7]

Oxynitrides are characterized by a mixed occupation of anionic sites by oxygen and nitrogen, bearing benefits for their use as energy materials in the following ways: (I) increasing the nitrogen content reduces the band gap of these n-type semiconductors, allowing them to absorb light in the visible wavelength range;[6] (II) the introduction of N 2p bands close to the valence band maximum shifts the band edges in favor of the potentials necessary to drive the water splitting half-reactions;[8] and (III) the changes in the electronic band

dispersion, for example, a modified curvature of the bands close to the Fermi level, can tune the kinetic properties of the charge carriers; this affects the initial charge carrier generation and transport in the semiconductor, both impacting the surface kinetics of the water splitting process.[4,9]

These arguments are favorable for the photoapplications of oxynitrides; however, under oxidative conditions of the OER, oxynitrides evince instability and are likely to lose nitrogen.[10] Nitrogen loss in oxynitrides has been directly observed by means of X-ray photoelectron spectroscopy (XPS),[11,12] ion scattering spectrometry, and transmission electron microscopy (TEM)[13] as well as by *in situ* gas chromatography[14−17] as direct evidence of the nitrogen evolution reaction running in parallel with the OER.[18,19] Notably, no prior study has linked the loss of nitrogen in oxynitrides during PEC to changes in their electronic properties, which are closely related to the water splitting efficiency and are therefore immensely more
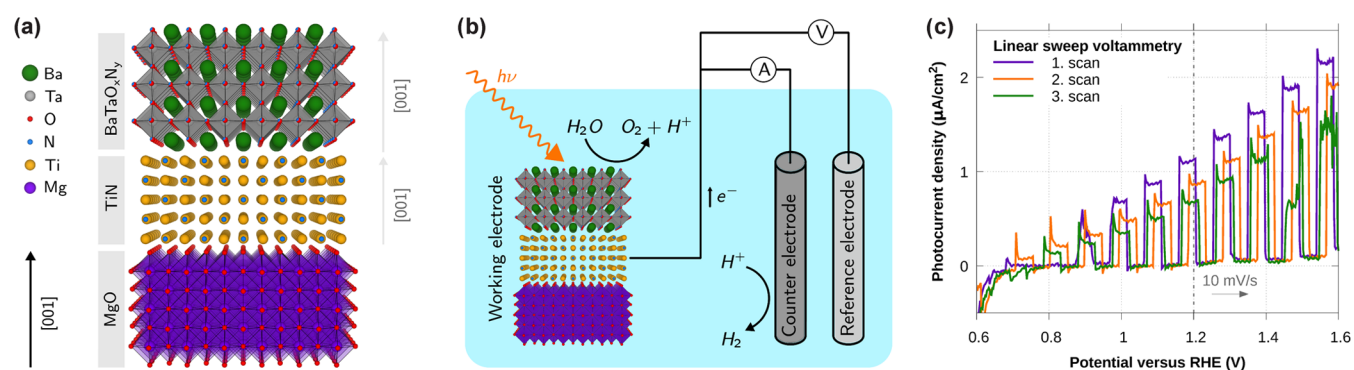
Figure 1. Oxynitride thin films and their photoelectrochemical operation. (a) Structural model of the BaTaO$_x$N$_y$ thin film system. (b) Schematic of the three-electrode configuration for photon($h\nu$)-induced water splitting, as explained in the Results section. (c) Three consecutive linear sweep voltammetric scans obtained from a BTON working electrode.
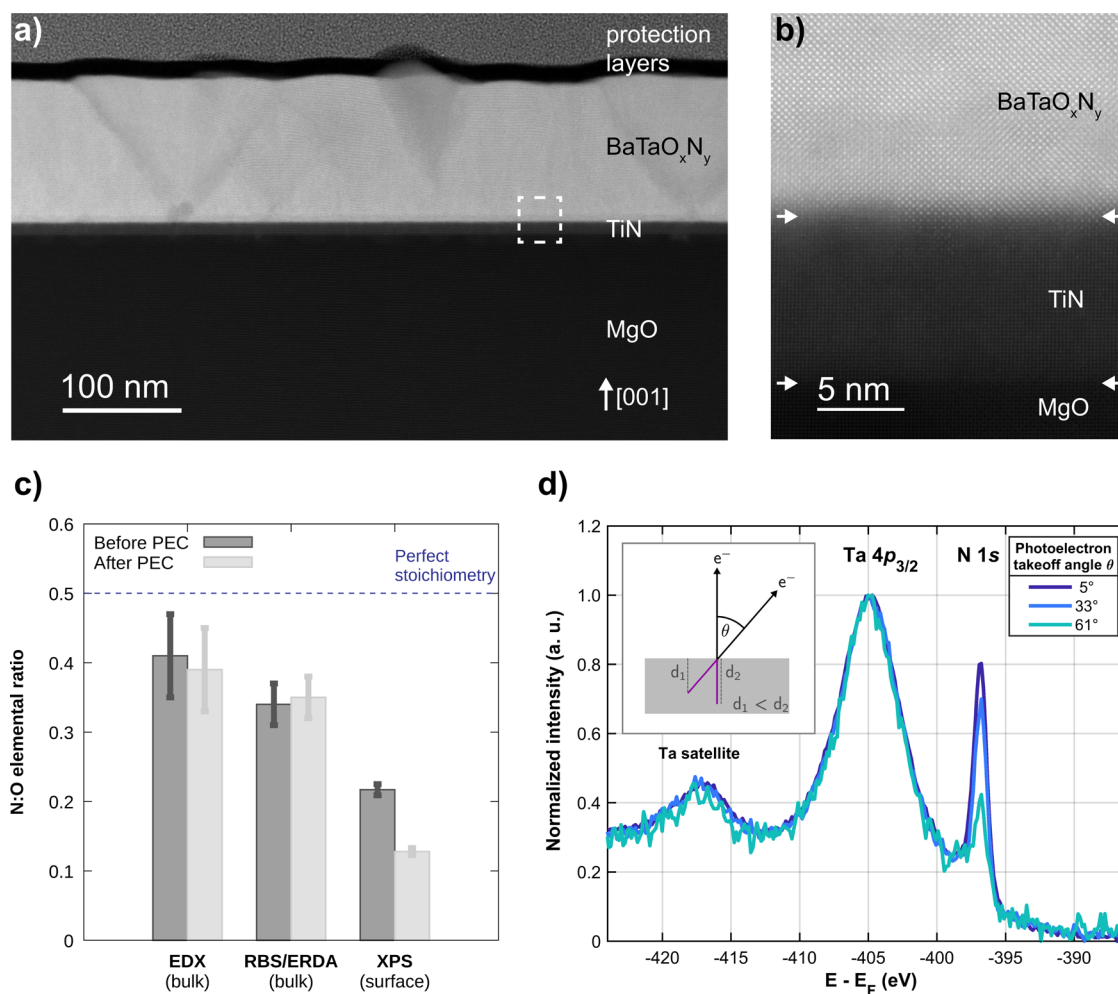

Figure 2. Structural and chemical analysis of the fabricated BaTaO$_x$N$_y$ thin film. (a) Low-magnification HAADF image of BaTaO$_x$N$_y$ before photoelectrochemistry (PEC) experiments. The protection layers were deposited for the TEM analysis only (Methods section). (b) Close-up section of the area denoted by the dashed box in panel (a), indicating the TiN-MgO and BaTaO$_x$N$_y$-TiN epitaxial interfaces with white arrows. (c) Elemental nitrogen-to-oxygen ratio (N:O) obtained from the oxynitride thin film before and after PEC using complementary techniques. (d) Angle-dependent XPS illustrating decreasing nitrogen abundance toward the surface (toward larger photoelectron takeoff angles) in a sample after PEC.

informative in the design of better-performing materials. Certainly, it is the skeleton composed of metal-anion bonds that determines the rich physical and chemical properties of perovskite-type oxides[20−22] and oxynitrides. We therefore aim to understand the impact of the anionic composition of

ABO$_2$N-type perovskite oxynitrides, where A and B represent the cations in the general formula, on their electronic structure and subsequently correlate it to their water splitting performance.

We consider the BaTaO$_x$N$_y$ (BTON) oxynitride (with $x = 2$ and $y = 1$ in the case of perfect stoichiometry) as a good candidate material due to a relatively small experimental band gap of ~1.9 eV[6,23] and suitable band edges for the production of oxygen (as well as hydrogen).[8,17] Consequently, BTON has been extensively investigated and characterized in the form of powders[24,25] and thin films[23] in the context of photo-electrochemistry during the past two decades.[6] Thin film samples offer the advantage of a defined surface, eliminating morphological effects[23] and allowing to study the intrinsic properties of the material. Thus, our work deals with thin film samples of epitaxially grown BTON with a (001) surface.

By combining transmission electron microscopy (TEM) and ion scattering techniques with photoemission spectroscopy (PES), we have elucidated the anionic composition of BTON(001) thin films as a function of the distance from the surface. Band structure computational modeling of the static disorder of anionic sites, in conjunction with our PES analysis, shows that deviations of the anionic content from ideal stoichiometry have detrimental consequences for the surface band structure of the oxynitride semiconductor. Correlated with the depth-dependent composition, our BTON samples evince downward band bending toward the surface, where band inversion leads to the loss of semi-conducting properties. Since this band bending effect extends over the majority of the expected space charge region, we argue that subtle changes in the anionic composition must have significant effects on the charge generation and charge transport during the OER, overall lowering the efficiency of BTON oxynitride photoanodes.

Our study reveals the surface metallicity of BTON oxynitrides and calls for a more detailed characterization of oxynitrides in terms of their composition and optoelectronic response in future research. We also suggest how the band structure of oxynitrides near the surface can be tuned to match the requirements for the reaction kinetics and the potential landscape that both drive the OER.

■ RESULTS

Thin Film Growth and Characterization. Thin film samples were fabricated by pulsed laser deposition and consisted of an insulating MgO(001) substrate, a conducting TiN buffer layer acting as the current collector with a thickness of approximately 10 nm, and an approximately 116 nm thick BTON oxynitride layer, which was epitaxially grown with the [001] crystallographic direction out-of-plane (Figure 1a). BTON crystallizes in the space group $Pm\overline{3}m$ (No. 221) and shows a simple cubic lattice as well as a simple cubic Brillouin zone in momentum space. The out-of-plane growth direction was confirmed by X-ray diffraction (see section S1 in the Supporting Information (SI)) and transmission electron microscopy (TEM). Thereby, high-angle annular dark-field (HAADF) images show the cross section of the multilayer system and its crystal quality in Figures 2a,b and S5 in the SI.

Photoelectrochemical Performance. Figure 1b illustrates how the BTON films work as photoanodes for the OER. The corresponding photoelectrochemical setup is briefly described below, with further experimental details provided in the Methods section. The PEC testing was performed in the three-electrode configuration, consisting of the working electrode, which is the BTON film system, the counter electrode, and the reference electrode, all immersed in an electrolyte and connected to a potentiostat. The potentiostat

sets the potential at the working electrode relative to the reference electrode (indicated by "V" in Figure 1b). Under solar radiation ("$h\nu$"), the generation of electron–hole pairs initiates water splitting. With applied positive bias, the generated electrons (e$^-$) in the oxynitride layer travel toward the TiN layer and further toward the counter electrode (photocathode), where the hydrogen evolution reaction takes place; simultaneously, the generated holes reach the oxynitride surface, where they drive the reactions of the OER and O$_2$ is produced.[5] Proportional to the production of molecular oxygen during water splitting, the photocurrent density of the photoanode can be measured to determine its efficiency (marked by "A" in Figure 1b).

Electrochemical testing of BTON photoanodes was conducted under chopped irradiation, collecting the photo-response of BTON thin films in terms of linear sweep voltammetry. The measured photocurrent density reached an average stabilized photocurrent of 1.12 μA cm^{-2} at 1.2 V versus reversible hydrogen electrode (RHE) for the first scan in Figure 1c and decreased gradually: it was diminished by ~39% in the third scan and resulted in an average stabilized photocurrent density of 0.47(7) μA cm^{-2} after the fifth scan until the last (ninth) scan. These results highlight the efficiency loss commonly observed for oxynitride photoanodes and are in line with reported PEC experiments using BaTaO$_x$N$_y$,[26] SrTaO$_x$N$_y$,[27] LaTiO$_x$N$_y$,[12,28,29] and CaNbO$_x$N$_y$[30] thin films.

Elemental Composition. The elemental composition of BTON before and after the electrochemical application was tracked by complementary techniques (see Figure 2c), which are either bulk- or surface-sensitive. Ion scattering techniques such as Rutherford backscattering (RBS) and heavy-ion elastic recoil detection analysis (ERDA) can give accurate values for the bulk elemental composition of thin films.[31] However, these techniques suffer from poor depth resolution when approaching the nm range. By using energy-dispersive X-ray (EDX) analysis, TEM allows to identify the bulk as well as the surface composition, even obtaining information about the N:O ratio for the top atomic layers close to the limit of the instrumental resolution, as represented by the large error bars in the SI, Figure S4. The most reliable technique for surface-sensitive studies is XPS. In the soft X-ray regime, an average probing depth of about 3–6 nm is obtained for perfectly stoichiometric BaTaO$_2$N using the TPP-2M formalism of the inelastic mean free path λ_{IMFP} of photoelectrons[32,33] and the average probing depth being equal to $3\lambda_{IMFP}$. The depth sensitivity can be tuned by varying the kinetic energy or the takeoff angle of emitted photoelectrons. The former can be adjusted via the incident photon energy ($h\nu$), and the latter is graphically visualized in the inset of Figure 2d.

While X-ray diffraction and TEM indicate no significant structural changes (SI, Figures S1–S5) of thin films before and after the PEC application, a change in the N:O ratio becomes evident for the BTON surface, as shown in Figure 2c. Qualitatively, this trend is reproduced by angle-dependent XPS (Figure 2d).

Anionic Disorder and Its Theoretical Implementation. Modeling atomic disorder can be challenging,[34] and several approaches have been developed over the past decades to implement static disorder in the frame of multiple-scattering theory.[35−37] For oxynitrides, recent computational approaches have suggested the atomic substitution of oxygen by nitrogen in an ordered fashion. This means that the nitrogen atoms preferentially occupy anionic sites, resulting in *cis*-type and
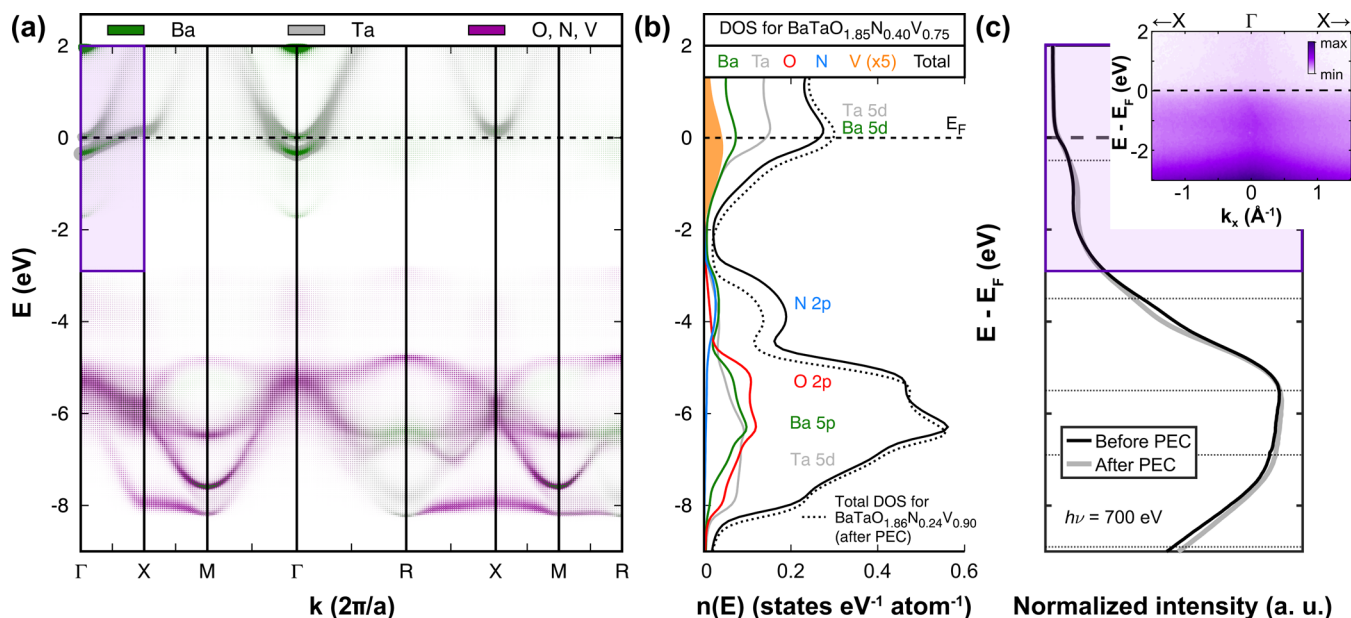
Figure 3. Computational and experimental features of the BTON band structure. (a) Site-dependent Bloch spectral function of $BaTaO_{1.85}N_{0.40}V_{0.75}$ with typical features of an anion-deficient oxynitride shown over characteristic momentum paths. The purple box marks the band structure region that has been explored experimentally, which is displayed in panel (c). (b) Total and partial density of states for the same system highlighting the main orbital contributions to the valence band region. The total density of states for $BaTaO_{1.86}N_{0.24}V_{0.90}$ corresponding to the composition after photoelectrochemistry (PEC) is represented by the black dotted line. (c) Experimental momentum-integrated photoemission spectrum for BTON before and after PEC. The inset shows the momentum-resolved data for the sample before PEC.

trans-type anion configurations[38−41] or even more complex scenarios.[42] Certainly, these local anionic arrangements could simplify the computational implementation of oxynitride systems. However, to the best of our knowledge, specific anion configurations have not been experimentally observed in thin films. We argue that local anion ordering cannot necessarily be applied to real samples with nonperfect stoichiometry, and since no studies performed to date have successfully shown direct experimental evidence of such anionic ordering, we considered a random distribution of anions. Using the SPR-KKR program package, we implemented such mixed occupancy sites in the frame of the coherent potential approximation (CPA) suitable for systems showing strong static disorder.[43] Herein, the anionic sites could host either host O, N, or vacancies V. Although we observe signs of a Ba-enriched surface in our XPS evaluation (see discussion in the SI, Section S6), for a first approximation analysis applicable to our soft X-ray probing depth, we consider a constant Ba:Ta ratio of 1 throughout the entire film corroborated by our TEM and RBS/ERDA results.

In the following paragraph, we explain the determination of BTON stoichiometries, including vacancy content, which we label as $V_{x'}^O$ and $V_{y'}^N$ in its stoichiometric formula, resulting in $BaTaO_{2-x}N_{1-y}V_{x'}^O V_{y'}^N$. Here, $V_{x'}^O$ represents the fraction of divalent oxygen removed from the crystal lattice. Likewise, $V_{y'}^N$ is the fraction of the removed nitrogen and is trivalent. Taking the valences of the anions and vacancies into consideration, their stoichiometric coefficients must sum up to −7 to conserve charge neutrality. We note that not all compositions resulting from this formula are stable and can be realized experimentally.

Nitrogen tends to leave the atomic lattice near the surface. Our angle-dependent XPS studies captured this loss due to the nitrogen evolution reaction in samples after the PEC (see Figure 2d). It seems that oxynitrides are characterized by a nitrogen-depleted surface, regardless of the surface treatment, which is mentioned in the SI, Section S8. This can be understood as follows: the lower bonding strength of the cations with nitrogen in comparison to oxygen leads to a band structure with N 2p states hybridizing at higher energies than the O 2p states,[6] as we will discuss later. Thus, we expect that most of the vacancies stem from nitrogen. In addition, it has been reported that vacancies can also stem from oxygen, and even complex interplays can exist.[44,45] Because there are several possible routes for the evolution of the anionic stoichiometry in BTON samples, further approximations to constrain the unknown coefficients are needed.

We obtain $O_{2-x'}$ and $V_{x'}^O$ based on the O:Ta ratio from XPS (see Table S2 in the SI). Further, the N:O ratio from XPS allows us to estimate $N_{1-y'}$ and $V_{y'}^N$. The resulting stoichiometries for our BTON sample are found to be $BaTaO_{1.85(5)}N_{0.403(18)}V_{0.147(4)}^O V_{0.597(27)}^N$ before PEC and $BaTaO_{1.86(5)}N_{0.239(11)}V_{0.138(4)}^O V_{0.76(3)}^N$ after PEC. For the sake of readability, these are referred to hereafter as $BaTaO_{1.85}N_{0.40}V_{0.75}$ and $BaTaO_{1.86}N_{0.24}V_{0.90}$, respectively.

First, we compared the electronic band structure in terms of the Bloch spectral function (BSF) representing the oxide phase $(BaTaO_{3.5})$ and the ideal oxynitride $(BaTaO_2N)$ in the SI, Figure S6a,b, respectively. While the oxide shows a well-defined valence band and a band gap of 3.5 eV, the band gap of the stoichiometric oxynitride is reduced to ∼1.7 eV. Furthermore, the valence band of the oxynitride is broadened over the momentum and energy ranges due to the inherent atomic disorder. This band smearing is most pronounced within the top 2 eV of the valence band and coincides with the energy range where the N 2p states become apparent in the representation of the density of states $n(E)$.

It remains to be a question for future work to elucidate how the broadening of the bands (the localization of valence electrons) is related to the initial charge carrier formation
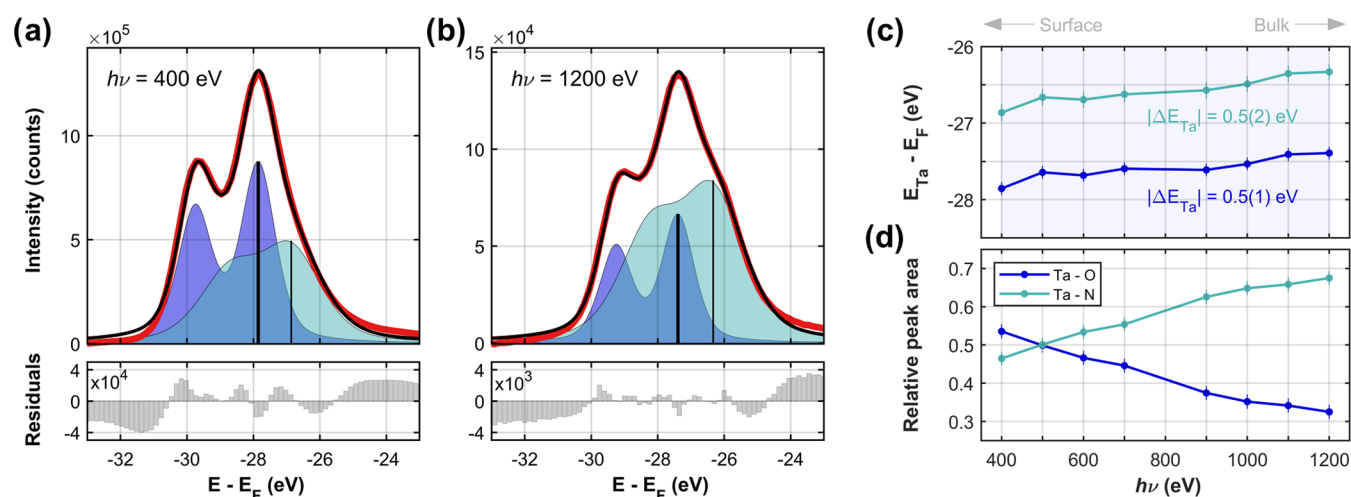
Figure 4. $h\nu$-dependent XPS with the Ta 4f core level of BaTaO$_x$N$_y$ after PEC. (a) Ta 4f core level characterized by the oxygen- (dark blue) and nitrogen- (light blue) derived doublet accessed with $h\nu = 400$ eV corresponding to the most surface-sensitive probing depth. The red line is the data, and the black one is the fit. (b) Ta 4f core level spectrum for $h\nu = 1200$ eV corresponding to most bulk-sensitive probing depth. (c) Extracted energies for both core level doublets as a function of the $h\nu$. $|\Delta E_{Ta}|$ gives the absolute change in energy for a core level over the used $h\nu$ range. (d) Relative contribution of each doublet to the fitted intensity of the Ta 4f core level as a function of the $h\nu$.

during PEC. The assignment of the Ta valence band states to Ta 5d classifies this material as a charge-transfer insulator according to the Mott−Hubbard model.[46] This type of electronic system can be prone to the loss of lattice anions, as discussed by Gent et al.[47] in terms of the oxygen redox of top valence band states and oxygen dimer formation in oxides.

To relate BSF computations to our real oxynitride samples, we implemented the determined oxygen, nitrogen, and vacancy contents in our computations. Figure 3 juxtaposes the calculated BSF and experimental band structure data from photoelectron spectroscopy (PES).

In comparison to perfectly stoichiometric BaTaO$_2$N, the introduction of anion-derived vacancies in BaTaO$_{1.85}$N$_{0.40}$V$_{0.75}$ affects both the valence and conduction band regions in terms of increased band smearing (Figure 3a) and the (SI, Figure S6c). The valence band states between −8 and −5 eV in Figure 3a show pronounced broadening and flattening of bands (highlighted by the purple anionic bands), indicating increased charge localization and enhanced effective hole masses, respectively. The latter must lower the mobility of holes in the oxynitride and impact its PEC performance.[4]

The valence band region between −5 and −3 eV in the off-stoichiometric BTON is predominantly occupied by N 2p hybridizing with the Ta 5d and Ba 5p states. In fact, these nondispersive cation-derived states populate the band gap region near both band edges. These in-gap states are reproduced in our experiments, whereby we observe a populated "band gap" below the Fermi level (E_F) in angle-resolved PES data (inset in Figure 3c). We expect that these Ta- and Ba-derived defect states appear due to the highly disordered charge environment around the cations caused by the defective anionic sublattice.

The vacancies present in BaTaO$_{1.85}$N$_{0.40}$V$_{0.75}$ also introduce new bands around the Γ point, located at around −1.8 eV in Figure 3a and highlighted in orange in Figure 3b. These bands were also accessed experimentally with PES (Figure 3c) and are faintly discernible in the angle-resolved data (inset in Figure 3c), centered around $k_x = 0$ Å^{-1}. The fact that those vacancy-derived bands are localized in momentum space means that the corresponding electrons are delocalized in real

space following the periodicity of the lattice. Again, we stress that the periodicity of the anionic sites was modeled using mixed occupancies and did not follow special local arrangements around the tantalum octahedra. The presence of these bands in the theoretical and experimental data supports our computational approach. Indeed, this agreement is an argument in favor of an in-plane random distribution of the O, N, and V species.

In addition, the total density of states for the system based on the BTON composition after PEC (BaTaO$_{1.86}$N$_{0.24}$V$_{0.90}$) was drawn into Figure 3b by the dashed line, which demonstrates a decreased population of N 2p states and an overall downward shift of the bands by −0.13 eV focusing on the predominant O 2p bands. This is in agreement with our experiments, where angle-integrated PES resolved a subtle ∼−0.15 eV global downward shift of the valence band for BTON after PEC in comparison to the sample before PEC (gray line in comparison to the black line in Figure 3c) as well as decreasing spectral weight for the feature located at $E − E_F$ = −3.5 eV. In total, these changes are minor, as can be expected from the valence band dominated by the spectral weight of barium (prevalence of the Ba 5p cross section[48]). Due to the absence of indicative shifts in energy for certain bands, we excluded notable changes in the degree of hybridization[49] between tantalum and the anions for this particular probing depth of ∼4 nm. This agrees with conclusions about the coordination environment for tantalum in SrTaO$_x$N$_y$ after PEC.[27]

Overall, anionic vacancies in BTON create excess electrons that occupy the in-gap states, inducing metallic behavior. This becomes apparent by the upward shift of E_F (or the downward shift of the band structure with respect to E_F) in our computations (Figure 3b) and experiments (Figure 3c). Figure 3 already indicates the changes of the band structure as a function of the anionic composition from a sample before and after PEC. For a better understanding of the electronic properties, we tracked the shifts of the band structure with respect to E_F for the BTON sample after PEC by means of XPS, described in the next section.

Band Bending at the Surface Region. In this section, we relate the anionic composition of BTON to the alignment of its original band edges as a function of depth using XPS. The extraction of the depth-dependent potential near the surface is, in general, nontrivial for PES in the valence band region.[50,51] This holds especially in our case, where a depth-specific anionic composition additionally modulates the states near E_F. Consequently, valence band leading edge fits must lead to erroneous results[50] for BTON samples. Thus, we accessed information about the surface band alignment of the oxynitride after PEC with $h\nu$-dependent XPS on the Ta 4f core level. We assume that a global shift in the energy of the BTON band structure translates to its core levels. For the core level region, we can also neglect considerable changes in the matrix elements as opposed to the matrix-element effects for the valence band region. We describe the fitting approach of the core levels in greater detail in the SI, Section S5.

The increase of the incident photon energy leads to an increase in the kinetic energy of the photoelectrons, allowing greater depths of the samples to be probed.[52] However, since the core level signal for a given $h\nu$ is a superposition of signals from all probed atomic layers following Beer–Lambert law,[53] the average probing depth cannot be set equal to the actual depth. This complicates the extraction of the depth-dependent band alignment represented by the Ta 4f core level energies. For a measurement at a certain $h\nu$, the depth can be estimated when the electrostatic potential is known.[50,53] Because no exact descriptions of potential profiles for oxynitride semiconductors exist, to our knowledge, we have established a description of the depth-dependent potential profile and the band profile in the SI, Section S9, based on nonuniform doping as a result of the change in anionic composition within the first 10 nm of BTON.

The Ta 4f core level consists of two doublets originating from the Ta–O (doublet at lower energies) and the Ta–N bonding environment. (See the SI, Section S7, for a discussion about the Ta 4f core-level assignment.) The fitted energy for each core level ($E_{Ta} - E_F$), exemplified by the vertical black lines in Figure 4a,b, as a function of $h\nu$, is displayed in Figure 4c. Here, a decrease for the Ta–O- and the Ta–N-derived core level energies toward more surface-sensitive $h\nu$ becomes apparent. This change in E_{Ta} across the probed $h\nu$ range is on the order of 0.5 eV for both core levels. In Figure 4d, we show the integrated peak areas for the Ta–O and Ta–N doublets. The almost linear decrease of the nitrogen-related peak area (Figure 4d) toward more surface-sensitive $h\nu$ indicates the loss of nitrogen. This is in agreement with the angle-dependent XPS study shown in Figure 2d.

Going from the bulk toward the surface of the BTON films, a gradual change in the anionic composition, exemplified by a decrease of the nitrogen and an increase of the vacancy content, induces n-doping, which is accompanied by downward band bending. We addressed this type of nonconstant doping across the space charge region in terms of linear n-doping, implemented in our model for a nonuniformly doped semiconductor in the SI, Section S9. This nonuniform doping results in an unusual band profile for depths up to 3 nm from the surface (Figure 5) in our obtained model. Applied to both Ta 4f core levels, the total band bending (or the band offset between the oxynitride and the vacuum region) is on the order of −0.6 eV.
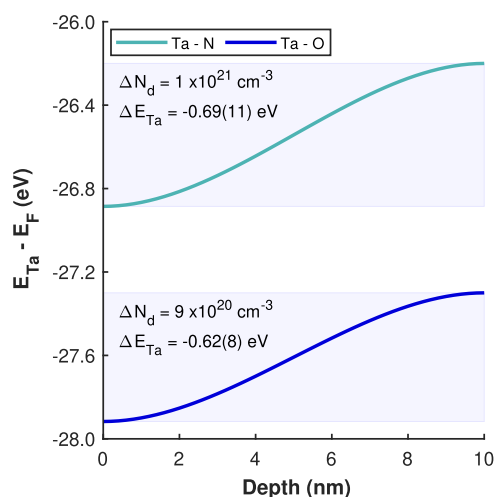

Figure 5. Representation of the Ta 4f core level of $BaTaO_xN_y$ after photoelectrochemistry as a function of depth, according to the model for nonuniform doping. The color-coded band profiles for both core-level doublets are based on our model using the best found value for ΔN_d (the linear change in dopant concentration across the space charge region). The resulting value for absolute band bending over the space charge region is also given with ΔE_{Ta}.

■ DISCUSSION

We quantified the N:O ratio in $BaTaO_xN_y$ oxynitride thin films before and after the described PEC application (*ex situ*) with complementary techniques. While no notable changes could be detected for the bulk composition using EDX and RBS/ERDA, XPS with $h\nu$ = 1100 eV allowed tracking of the decrease in the N:O ratio by ~41% for BTON after the PEC. Our core level analysis also suggests that part of the anionic vacancies in BTON samples are replaced by oxygen during the OER and that the higher electronegativity of oxygen ensures the pentavalent oxidation state of tantalum. Another indication that this happens in BTON samples is the prevalence of the Ta–O contribution to the Ta 4f core level toward the surface (see Figure 4d).

Based on the XPS results, the anionic composition of BTON samples was determined as an integrand value over the probing depth for the actual $h\nu$ and was implemented in our band structure calculations. The computational results are in qualitative agreement with the spectral features in angle-integrated PES. As discussed above, the BTON band structure is characterized by features arising from the static anionic disorder. Most notably, the loss of N 2p valence band states, exposing the cation (defect) states, is accompanied by the shift of E_F.

$h\nu$-dependent XPS of the Ta 4f core level for the BTON sample after PEC evinced a chemical gradient in terms of a decreasing N:O ratio toward the surface and a shift of the fitted energies across the experimentally accessible probing depth. Based on these compositional changes, the established model description for nonuniformly doped BTON enabled a band profile for the Ta 4f core level with depth. The observed downward band bending in the order of −0.6 eV can be expected for systems after surface treatment.[54,55]

Based on these observations for BTON, we now address how the electronic structure relates to the semiconductor physics and its PEC performance. The vacancies in a real and defective BTON system induce band structure characteristics

and have a detrimental influence on the electronic and functional properties.

(I) Anionic vacancies in the oxynitride create excess electrons that lead to charge accumulation in the n-type semiconductor. In a simple band diagram, this leads to a downward band bending toward the surface. According to the model used for nonuniformly doped oxynitrides, one can expect a built-in field leading to band bending under equilibrium conditions, which is opposed to the customary representation of oxynitrides under flat band conditions. Within the band bending region of our sample, the position of the Fermi level for our nonstoichiometric oxynitride (Figure 3) is expected to be above the conduction band minimum of a stoichiometric oxynitride as displayed in Figure S6b.[8] This is characteristic for a degenerate n-type semiconductor and agrees with the relatively high dopant concentrations from the band bending analysis mentioned in Figure 5. The resulting band inversion leads to surface metallicity and a decrease in the photocurrent. This type of band alignment is undesired for the photoanodes and must be overcome during PEC. Conversely, upward band bending facilitates the transport of holes to the surface, where they "feed" the charge transfer processes for the OER. (II) Emerging in-gap states must considerably contribute to the charge carrier recombination, further decreasing the photocurrent. (III) Surpassing a critical density of in-gap states, the oxynitride semiconductor turns into a metal and possibly loses its function as a photoactive material.

Notably, BTON shows only little modification in terms of its crystal structure across the PEC. In additional experiments (not reported), we were able to grow epitaxial BTON films even for low nitrogen contents (with N:O < 1% according to XPS with $h\nu$ = 1100 eV). The fact that the simple cubic lattice persists at strongly defective anionic compositions highlights the exceptional structural stability of the lattice. Likely, further oxidation of the compound in the frame of the OER must introduce lattice instability exceeding strain effects, as discussed in the SI, Section S1, and structural decomposition. The spectral weight of the in-gap states, as seen in PES, could therefore be a precursor state of BTON before its lattice breaks down. Indeed, we hypothesize that the structural robustness of BTON prevents charge compensation and promotes in-gap states. To overcome this intrinsic problem, we share strategies to overcome charge imbalances from a materials design perspective in the following paragraph.

In general, the electronic properties for idealized photoactive oxynitrides, such as those found in computational analyses, can only be achieved in a perfectly stoichiometric structure. In real systems, however, anionic vacancies will most likely be present. To compensate this charge imbalance and thereby improve the electronic properties of oxynitride photoanodes, the priority must be to grow samples with the highest nitrogen content possible, approaching perfect stoichiometry while maintaining a high crystal quality. In case sufficient nitrogen incorporation cannot be attained, we suggest the following routes: (I) intrinsic p-doping, instead of n-doping,[56] by A and B site cations, resulting in a monovalent cation (such as K^+, Na^+, Li^+, or Ag^+) for the A site or a tetravalent cation (such as Ti^{4+}, Zr^{4+}, Hf^{4+}, or Sn^{4+}) for the B site,[57] in the case of BTON; (II) p-doping by the fabrication of heterostructures, including $A(O,N)_1$ and $B(O,N)_2$ layers, where A and B stand for the aforementioned cations in the case of BTON; and/or (III) employing oxynitrides with more flexible structural frameworks. For the latter, octahedral tilting and cationic displace-

ments could counterbalance excess electrons in the semiconductor. Herein, the proposed ABO_2N-type compounds with orthogonal conventional bases, such as orthorhombic, tetragonal, and cubic crystal systems, and octahedral tilting in one, two, or even three crystallographic directions, could be used. Common examples for these three tilt systems are $SrTaO_2N$, $SrNbO_2N$ with space group $I4/mcm$ (No. 140), $LaTaO_2N$ and $LaTiO_2N$ with $Imma$ (No. 74), and $CaTaO_2N$, $CaNbO_2N$, $CaMoO_2N$, $CeNbO_2N$, $LaZrO_2N$, and $NdTiO_2N$ with $Pnma$ (No. 62), respectively. However, tilting can increase the phonon-mediated charge transport, thereby inhibiting hole transport in the semiconductor. Thus, one must be careful when optimizing the system.

In addition to the suggested improvements for the photoresponse of oxynitrides, one needs to boost their catalytic properties. Species possessing higher OER activity such as transition metal oxides should be introduced, for example, as a top cocatalyst.[24,29,58] Top metal oxides could further aid in the passivation of the surface[59,60] and counteract the preferred oxidation of BTON. We expect the above-mentioned points to be transferable to other commonly studied oxynitrides, such as $SrTaO_xN_y$, $LaTiO_xN_y$, and $CaNbO_xN_y$.

CONCLUSIONS

We have elucidated the characteristic band structures of real oxynitride thin films with defective anionic compositions and contributed to a depth-dependent and in-depth understanding of the oxynitride band structures and their evolution across the PEC.

For oxynitrides, we expect that the OER runs in parallel with the nitrogen evolution reaction, involving the loss of lattice nitrogen. This reaction has been detected in past experiments with powders[14−17] and films[27,29] but was usually considered to be of negligible significance. Our investigation of the electronic structure of BTON samples, however, proved the opposite and revealed the detrimental consequences of nitrogen loss and anionic disorder of oxynitrides in general: anionic deficiencies can even lead to the loss of the semiconductor properties at the surface, where inversion of the n-type semiconductor turns the compound into a metal and must consequently hinder the electron−hole pair formation. In such a case, the desired characteristics of photoactive oxynitrides are lost.

Finally, the electronic properties of an oxynitride semiconductor are inherently tied to its anionic stoichiometry and need to be addressed before "trial-and-error" engineering of oxynitride films and powders. Our work has investigated the very basic properties of BTON, and therefore forms a basis for tuning the electronic structure of oxynitride photoelectrodes through future studies with angle-resolved PES.

METHODS

Pulsed Laser Deposition of Oxynitride Thin Films. For each pulsed laser deposition, a 10 × 10 mm² large MgO(001) substrate (CrysTec GmbH) was used. To facilitate several sample characterizations for the same batch, we cut each MgO substrate into four equally sized pieces. All data discussed in this publication stem from a single sample batch. Only the angle-dependent XPS data originate from separate batches produced under the same experimental conditions.

The cut 5 × 5 mm² substrates were sonicated for 15 min in acetone, followed by 15 min long sonication in propan-2-ol before thermal annealing in a tube furnace at 1000 °C for 12 h. The heating ramp of the tube furnace was 5.8 °C min⁻¹ and cooling proceeded in a passive manner.

The substrates were mounted on a substrate holder with Ag paste (SPI Supplies, Structure Probe Inc.), which was cured in a stepwise fashion (50−120 °C) for at least 45 min. The substrate holder was then introduced into the deposition chamber and gradually heated to 700 °C. We note that sufficiently high temperatures at the substrate are crucial for crystal quality and nitrogen incorporation during deposition.

Thin film systems were fabricated using a pulsed KrF excimer laser (LPX305iCC, Lambda Physik), with $\lambda = 248$ nm and a measured fluence of 2.3 J cm^{-2}; ablating material from a rod-shaped target that was positioned 50 mm away from the sample substrate. A TiN target was ablated for 30 min with a set laser frequency of 10 Hz while the pressure was kept at $2 \cdot 10^{-6}$ mbar. This was followed by a 30 min long ablation of a $Ba_5Ta_4O_{15}$ target with the frequency of 7 Hz. In this step, a nitrogen and ammonia gas mixture, with a molar $NH_3:N_2$ ratio of 1:2/3, served as the background gas to create the reducing environment necessary for oxynitride production.[61] The total pressure in the chamber during deposition was 2×10^{-6} mbar.

Photoelectrochemical Testing. PEC measurements were executed in a three-electrode configuration consisting of an Ag/AgCl reference electrode (stored in saturated KCl), a Pt counter electrode, and the BTON working electrode attached to a TiN-coated stainless steel wire. We used a custom-designed reactor cell[27] of polyether ether ketone (PEEK) with 190 μm thick Mylar foil as the window. The cell was filled with a 0.5 M NaOH aqueous electrolyte solution.

A 50−500 W xenon DC arc lamp (Oriel Instruments, Newport) with a 69907 Universal Arc Lamp Power Support (Newport) was employed as the light source. Hereby, a lens and XLP12 power detector system (Gentec) in conjunction with the PC interface and software Integra (Gentec-EO) helped to define incoming light of 100 mW cm^{-2} (equal to 1 sun).

Linear sweep voltammograms were collected at room temperature (25 °C) between 0.6 and 1.6 V versus RHE with a scan rate of 10 mV s^{-1} with the μAutolab type III/FRA2 (Metrohm Autolab) potentiostat using the software Nova. The initial (zeroth) potentiodynamic scan was executed under dark conditions (not shown in Figure 1c), followed by measurements under chopped illumination with a period of 3 s.

The potential $E_{Ag/AgCl}$ measured against the reference electrode with $E^0_{Ag/AgCl}$ was converted to the potential versus RHE (E_{RHE}), as shown in Figure 1c, via the Nernst equation $E_{RHE} = E^0_{Ag/AgCl} + 0.05916 \cdot pH + E_{Ag/AgCl}$. Taking the pH value of the electrolyte ($pH_{0.5MNaOH} = 13.55$) and the sample area in contact with the electrolyte into account, the current−potential curves, as shown in Figure 1c, were obtained.

For comparison, we enlist the values of the measured photocurrent normalized with respect to the sample surface at 1.2 V versus the RHE potential, as marked by the dashed line in Figure 1c. We performed the PEC experiments on three BTON samples grown under comparable deposition conditions, giving a mean value of 1.02(20) μA cm^{-2} for the first linear sweep voltammetric scan. While one of the samples did not give a further response after the first cycle, the other two samples showed average values of 0.93(4) and 0.82(14) μA cm^{-2} for the second and third scans, respectively. We note that it was not possible to determine the sample surface exposed to the electrolyte in the submillimeter-regime. Herein, possible fluctuations of the meniscus at the electrolyte-sample-air interface must lead to non-negligible deviations. The photocurrent was also not iR corrected. For the quantification of the PEC performance, however, we propose extended tests and long-term cycling.

The photocurrent density stabilizes after the fifth scan, where it reaches an average "stabilized" photocurrent density[12,26] (averaged over the sixth until the ninth scan) of 0.47(7) μA cm^{-2}.

The so-called "recombination peaks," which are the spikes at the onset of the photocurrent steps in Figure 1c, commonly observed for oxynitrides,[12,24,27,29,30] are more pronounced when the light is turned on than off. This asymmetry suggests that more complex mechanisms, besides the recombination of surface holes, are involved.[62]

Transmission Electron Microscopy. Protection layers were deposited on the BTON surfaces for electron microscopy (sample preparation and imaging): from the BTON film to the sample surface, the thin protective layers consist of ~10 nm amorphous carbon (dark layer in Figure 2a) and ~100 nm Pt (thicker top gray layer in Figure 2a) as well as further ~1600 nm Pt (not shown in Figure 2a) deposited with an electron beam and ion beam, respectively. TEM specimens were prepared via the focused ion beam lift-out technique using a Thermo Fisher Scientific Helios 4UC instrument operated at 30 kV, and final cleaning was performed at 5 and 2 kV. High-angle annular dark-field (HAADF) images and EDX maps (see the SI, Figure S3) were collected with a Themis Z 3.1 60−300 FEG Scanning transmission electron microscope (STEM) operated at 300 kV, which was equipped with a Gatan Imaging Filter Continuum 1065 and a SuperX energy-dispersive X-ray detector.

Ion Scattering Techniques. Rutherford backscattering (RBS) and heavy-ion elastic recoil detection analysis (ERDA) elemental analyses were carried out at the 1.7 MV Tandetron accelerator facility located at the Ion Beam Physics Laboratory at ETH Zurich, Switzerland. RBS was conducted with a 2 MeV ^{4}He beam. For detection of the backscattered ions, a Si PIN diode was used. The corresponding data was analyzed using the RUMP program.[63] To detect the relatively light oxygen and nitrogen atoms in the sample, heavy-ion elastic recoil detection analysis (ERDA) with a 13 MeV ^{127}I beam with 18 deg incident and exit angle, a time-of-flight spectrometer, and gas ionization detector was performed. The depth profiles were analyzed with Potku software.[64]

Photoelectron Spectroscopy. All PES experiments were performed at the soft X-ray ARPES endstation[65] as part of the ADRESS beamline[52] at the Swiss Light Source, PSI, Switzerland. Measurements benefited from the high flux up to 10^{13} photons·s^{-1}·0.01%BW^{-1} and a broad accessible photon energy range of $h\nu = 300−1600$ eV. The temperature of the sample was approximately 14 K for all measurements. p-polarized light was used for the core level measurements, and right-circularly polarized light was used for the angle-integrated and angle-resolved measurements in the valence band region, as shown in Figure 3c. The combined energy resolution resulting from the beamline and the hemispherical analyzer (PHOIBOS-150) varied with photon energy from ~40 meV ($h\nu = 400$ eV) to ~147 meV ($h\nu = 1200$ eV) for XPS measurements. The corresponding resolution for the valence band spectroscopy with $h\nu = 700$ eV was <120 meV. Information about the sample preparation can be found in the SI, Section S8.

Details about the Electronic Structure Calculations. Calculations were performed with the Korringa−Kohn−Rostoker (KKR) multiple-scattering method as implemented in the SPR-KKR package.[66] This Green's function-based approach allowed a fully relativistic treatment of the BTON system with varying anionic composition. First-principles calculations in the frame of density functional theory (DFT) were executed using the modified Becke Johnson (mBJ) exchange−correlation functional,[67,68] which is a meta generalized gradient approximation (meta-GGA) potential suitable for perovskite-type structures and the description of optical properties in semiconductors.[43] The self-consistent-field (SCF) potential of the BTON systems was obtained in the atomic-sphere approximation (ASA) mode as an appropriate description for perovskite-type correlated oxide systems.[51] The cubic lattice parameter $a = 4.113$ Å (ICSD #258747) was used for all computations.[69] The angular-momentum cutoff was set to 4, and the magnetic effective field was set to zero. Including spin−orbit coupling, we obtained band hybridization exemplified by Ta 5d states close to the conduction band minimum (for $BaTaO_2N$) at Γ and O 2p states close to 3.5 eV at the R point. We ensured that the convergence parameters for the KKR structure constant matrix match the converging solution of systematic, cluster-size-dependent studies on the structure constant matrix for KKR computations in the tight binding mode. Atomic disorder of the anionic sites, occupied by oxygen, nitrogen, or vacancies, was implemented within the coherent potential approximation (CPA) in SPR-KKR.[66]

The Bloch spectral function (BSF), as the Fourier transform of the retarded Green's function in real space, allowed understanding the characteristic oxynitride band dispersion through high-symmetry points of the simple cubic Brillouin zone (see Figure 3a) and the (SI, Figure S6). The BSF can be seen as the **k**-resolved ground state density of states whereby the imaginary energies in the description of the BSF cause the broadening of bands.[34,66] The partial density of states used for (Figure 3b) was obtained by the integration of over 500 **k**-points. We discuss and justify our computational approach in greater detail in the SI, Section S3.

■ ASSOCIATED CONTENT

Data Availability Statement

Additional data consisting of PES raw data files in *.h5 format, the results from RBS/ERDA measurements, and the quantification of the N:O ratio using TEM, as shown in the SI, Figure S4, are summarized at the Zenodo open data repository accessible via 10.5281/zenodo.13350672.

Supporting Information

The Supporting Information is available free of charge at https://pubs.acs.org/doi/10.1021/acs.chemmater.4c01832.

> Further sample characterization by means of X-ray diffraction, TEM, and PES; explanations concerning the computational approach; the PES data processing as well as the PES sample preparation; and the derivation of the model for nonuniformly doped oxynitrides (PDF)

■ AUTHOR INFORMATION

Corresponding Authors

Vladimir N. Strocov − *Center for Photon Science, Paul Scherrer Institute, 5232 Villigen PSI, Switzerland;* orcid.org/0000-0002-1147-8486; Email: vladimir.strocov@psi.ch

Nick A. Shepelin − *Center for Neutron and Muon Sciences, Paul Scherrer Institute, 5232 Villigen PSI, Switzerland;* orcid.org/0000-0002-5446-9213; Email: nikita.shepelin@psi.ch

Authors

Anna Hartl − *Center for Neutron and Muon Sciences, Paul Scherrer Institute, 5232 Villigen PSI, Switzerland; Center for Photon Science, Paul Scherrer Institute, 5232 Villigen PSI, Switzerland; Laboratory of Inorganic Chemistry, Department of Chemistry and Applied Biosciences, ETH Zürich, 8093 Zurich, Switzerland*

Ján Minár − *New Technologies-Research Center, University of West Bohemia, 301 00 Plzeň, Czech Republic*

Procopios Constantinou − *Center for Photon Science, Paul Scherrer Institute, 5232 Villigen PSI, Switzerland;* orcid.org/0000-0001-9769-9345

Vladimir Roddatis − *GFZ German Research Centre for Geosciences, 14473 Potsdam, Germany;* orcid.org/0000-0002-9584-0808

Fatima Alarab − *Center for Photon Science, Paul Scherrer Institute, 5232 Villigen PSI, Switzerland*

Arnold M. Müller − *Laboratory of Ion Beam Physics, Department of Physics, ETH Zürich, 8093 Zurich, Switzerland*

Christof Vockenhuber − *Laboratory of Ion Beam Physics, Department of Physics, ETH Zürich, 8093 Zurich, Switzerland*

Thorsten Schmitt − *Center for Photon Science, Paul Scherrer Institute, 5232 Villigen PSI, Switzerland*

Daniele Pergolesi − *Center for Neutron and Muon Sciences, Paul Scherrer Institute, 5232 Villigen PSI, Switzerland;* orcid.org/0000-0002-6231-0237

Thomas Lippert − *Center for Neutron and Muon Sciences, Paul Scherrer Institute, 5232 Villigen PSI, Switzerland; Laboratory of Inorganic Chemistry, Department of Chemistry and Applied Biosciences, ETH Zürich, 8093 Zurich, Switzerland;* orcid.org/0000-0001-8559-1900

Complete contact information is available at:
https://pubs.acs.org/10.1021/acs.chemmater.4c01832

Notes

The authors declare no competing financial interest.

■ REFERENCES

(1) Fujishima, A.; Honda, K. Electrochemical Photolysis of Water at a Semiconductor Electrode. *Nature* **1972**, *238*, 37−38.

(2) Khaselev, O.; Turner, J. A. A monolithic photovoltaic-photoelectrochemical device for hydrogen production via water splitting. *Science* **1998**, *280*, 425−427.

(3) Crabtree, G. W.; Dresselhaus, M. S.; Buchanan, M. V. The hydrogen economy. *Phys. Today* **2004**, *57*, 39−44.

(4) Qiu, J.; Nellist, M. R.; Boettcher, S. W. *Ultrathin Oxide Layers for Solar and Electrocatalytic Systems*; The Royal Society of Chemistry, 2022; Chapter 6, pp 135−166.

(5) Seh, Z. W.; Kibsgaard, J.; Dickens, C. F.; Chorkendorff, I.; Nørskov, J. K.; Jaramillo, T. F. Combining theory and experiment in electrocatalysis: Insights into materials design. *Science* **2017**, *355*, No. eaad4998.

(6) Maeda, K.; Domen, K. New non-oxide photocatalysts designed for overall water splitting under visible light. *J. Phys. Chem. C* **2007**, *111*, 7851−7861.

(7) Takata, T.; Jiang, J.; Sakata, Y.; Nakabayashi, M.; Shibata, N.; Nandal, V.; Seki, K.; Hisatomi, T.; Domen, K. Photocatalytic water splitting with a quantum efficiency of almost unity. *Nature* **2020**, *581*, 411−414.

(8) Balaz, S.; Porter, S. H.; Woodward, P. M.; Brillson, L. J. Electronic structure of tantalum oxynitride perovskite photocatalysts. *Chem. Mater.* **2013**, *25*, 3337−3343.

(9) Mills, T. J.; Laskowski, F. A. L.; Dette, C.; Nellist, M. R.; Lin, F.; Boettcher, S. W. The Role of Surface States in Electrocatalyst-Modified Semiconductor Photoelectrodes: Theory and Simulations. 2017, arXiv:1707.03112. arXiv.org e-Printarchive. https://arxiv.org/abs/1707.03112. (accessed November 4, 2024).

(10) Chen, S.; Wang, L. W. Intrinsic defects and electronic conductivity of TaON: First-principles insights. *Appl. Phys. Lett.* **2011**, *99*, No. 222103.

(11) Abe, R.; Higashi, M.; Domen, K. Facile fabrication of an efficient oxynitride TaON photoanode for overall water splitting into H2 and O2 under visible light irradiation. *J. Am. Chem. Soc.* **2010**, *132*, 11828−11829.

(12) Pichler, M.; Si, W.; Haydous, F.; Téllez, H.; Druce, J.; Fabbri, E.; Kazzi, M. E.; Döbeli, M.; Ninova, S.; Aschauer, U.; Wokaun, A.; Pergolesi, D.; Lippert, T. LaTiOxNy Thin Film Model Systems for Photocatalytic Water Splitting: Physicochemical Evolution of the Solid−Liquid Interface and the Role of the Crystallographic Orientation. *Adv. Funct. Mater.* **2017**, *27*, No. 1605690.

(13) Therani, Z. P. Developing Characterization Strategies for Photocatalytic Oxynitrides: A Case Study for SrTaO2N, Doctoral dissertation; ETH Zurich, 2022.

(14) Kasahara, A.; Nukumizu, K.; Hitoki, G.; Takata, T.; Kondo, J. N.; Hara, M.; Kobayashi, H.; Domen, K. Photoreactions on LaTiO2N under visible light irradiation. *J. Phys. Chem. A* **2002**, *106*, 6750−6753.

(15) Takata, T.; Hitoki, G.; Kondo, J. N.; Hara, M.; Kobayashi, H.; Domen, K. Visible-light-driven photocatalytic behavior of tantalum-oxynitride and nitride. *Res. Chem. Intermed.* **2007**, *33*, 13−25.

(16) Black, A. P.; Suzuki, H.; Higashi, M.; Frontera, C.; Ritter, C.; De, C.; Sundaresan, A.; Abe, R.; Fuertes, A. New rare earth hafnium oxynitride perovskites with photocatalytic activity in water oxidation and reduction. *Chem. Commun.* **2018**, *54*, 1525−1528.

(17) Luo, Y.; Suzuki, S.; Wang, Z.; Yubuta, K.; Vequizo, J. J. M.; Yamakata, A.; Shiiba, H.; Hisatomi, T.; Domen, K.; Teshima, K. Construction of Spatial Charge Separation Facets on BaTaO2N Crystals by Flux Growth Approach for Visible-Light-Driven H2 Production. *ACS Appl. Mater. Interfaces* **2019**, *11*, 22264−22271.

(18) Higashi, M.; Domen, K.; Abe, R. Fabrication of an efficient BaTaO2N photoanode harvesting a wide range of visible light for water splitting. *J. Am. Chem. Soc.* **2013**, *135*, 10238−10241.

(19) Ouhbi, H.; Aschauer, U. Nitrogen Loss and Oxygen Evolution Reaction Activity of Perovskite Oxynitrides. *ACS Mater. Lett.* **2019**, *1*, 52−57.

(20) Hwang, J.; Rao, R. R.; Giordano, L.; Katayama, Y.; Yu, Y.; Shao-Horn, Y. Perovskites in catalysis and electrocatalysis. *Science* **2017**, *358*, 751−756.

(21) Strocov, V. N.; Lechermann, F.; Chikina, A.; Alarab, F.; Lev, L. L.; Rogalev, V. A.; Schmitt, T.; Husanu, M. A. Dimensionality of mobile electrons at x-ray-irradiated LaAlO3/SrTiO3 interfaces. *Electron. Struct.* **2022**, *4*, No. 015003.

(22) Plumb, N. C.; Radović, M. Angle-resolved photoemission spectroscopy studies of metallic surface and interface states of oxide insulators. *J. Phys.: Condens. Matter* **2017**, *29*, No. 433005.

(23) Haydous, F.; Döbeli, M.; Si, W.; Waag, F.; Li, F.; Pomjakushina, E.; Wokaun, A.; Gökce, B.; Pergolesi, D.; Lippert, T. Oxynitride thin films versus particle-based photoanodes: A comparative study for photoelectrochemical solar water splitting. *ACS Appl. Energy Mater.* **2019**, *2*, 754−763.

(24) Ueda, K.; Minegishi, T.; Clune, J.; Nakabayashi, M.; Hisatomi, T.; Nishiyama, H.; Katayama, M.; Shibata, N.; Kubota, J.; Yamada, T.; Domen, K. Photoelectrochemical oxidation of water using BaTaO2N photoanodes prepared by particle transfer method. *J. Am. Chem. Soc.* **2015**, *137*, 2227−2230.

(25) Hojamberdiev, M.; Mora-Hernandez, J. M.; Vargas, R.; Yamakata, A.; Yubuta, K.; Heppke, E. M.; Torres-Martínez, L. M.; Teshima, K.; Lerch, M. Time-retrenched synthesis of BaTaO2N by socalizing an NH3 delivery system for visible-light-driven photo-electrochemical water oxidation at neutral pH: solid-state reaction or flux method? *ACS Appl. Energy Mater.* **2021**, *4*, 9315−9327.

(26) Haydous, F. Thin Film and Powder-Based Semiconductor Photoanodes for Visible Light-Induced Water Splitting; Ph.D. thesis, ETH Zurich, 2018.

(27) Lawley, C.; Tehrani, Z. P.; Clark, A. H.; Safonova, O. V.; Döbeli, M.; Strocov, V. N.; Schmidt, T. J.; Lippert, T.; Nachtegaal, M.; Pergolesi, D. Protagonists and spectators during photocatalytic solar water splitting with SrTaOxNy oxynitride. *J. Mater. Chem. A* **2022**, *10*, 2374−2387.

(28) Burns, E.; Aschauer, U.; Döbeli, M.; Schneider, C. W.; Pergolesi, D.; Lippert, T. LaTiO2N crystallographic orientation control significantly increases visible-light induced charge extraction. *J. Mater. Chem. A* **2020**, *8*, 22867−22873.

(29) Lawley, C.; Nachtegaal, M.; Stahn, J.; Roddatis, V.; Döbeli, M.; Schmidt, T. J.; Pergolesi, D.; Lippert, T. Examining the surface evolution of LaTiOxNy an oxynitride solar water splitting photo-catalyst. *Nat. Commun.* **2020**, *11*, No. 1728.

(30) Haydous, F.; Luo, S.; Wu, K. T.; Lawley, C.; Döbeli, M.; Ishihara, T.; Lippert, T. Surface analysis of perovskite oxynitride thin films as photoelectrodes for solar water splitting. *ACS Appl. Mater. Interfaces* **2021**, *13*, 37785−37796.

(31) Döbeli, M.; Kottler, C.; Glaus, F.; Suter, M. ERDA at the low energy limit. *Nucl. Instrum. Methods Phys. Res., Sect. B* **2005**, *241*, 428−435.

(32) Tanuma, S.; Powell, C. J.; Penn, D. R. Proposed formula for electron inelastic mean free paths based on calculations for 31 materials. *Surf. Sci.* **1987**, *192*, L849−L857.

(33) Shinotsuka, H.; Tanuma, S.; Powell, C. J.; Penn, D. R. Calculations of electron inelastic mean free paths. XII. Data for 42 inorganic compounds over the 50 eV to 200 keV range with the full Penn algorithm. *Surf. Interface Anal.* **2019**, *51*, 427−457.

(34) Minár, J.; Mankovsky, S.; Šipr, O.; Benea, D.; Ebert, H. Correlation effects in fcc-FexNi1-x alloys investigated by means of the KKR-CPA. *J. Phys.: Condens. Matter* **2014**, *26*, No. 274206.

(35) Bellaiche, L.; Vanderbilt, D. Virtual crystal approximation revisited: Application to dielectric and piezoelectric properties of perovskites. *Phys. Rev. B* **2000**, *61*, 7877−7882.

(36) Bansil, A. Coherent-potential and average t-matrix approximations for disordered muffin-tin alloys. I. Formalism. *Phys. Rev. B* **1979**, *20*, No. 4025.

(37) Soven, P. Coherent-potential model of substitutional disordered alloys. *Phys. Rev.* **1967**, *156*, 809−813.

(38) Lan, Z.; Vegge, T.; Castelli, I. E. Theoretical Insight on Anion Ordering, Strain, and Doping Engineering of the Oxygen Evolution Reaction in BaTaO2N. *Chem. Mater.* **2021**, *33*, 3297−3303.

(39) Ouhbi, H.; Aschauer, U. Water oxidation chemistry of oxynitrides and oxides: Comparing NaTaO3 and SrTaO2N. *Surf. Sci.* **2018**, *677*, 258−263.

(40) Garcia-Castro, A. C.; Ma, Y.; Romestan, Z.; Bousquet, E.; Cen, C.; Romero, A. H. Engineering of Ferroic Orders in Thin Films by Anionic Substitution. *Adv. Funct. Mater.* **2022**, *32*, No. 2107135.

(41) Page, K.; Stoltzfus, M. W.; Kim, Y. I.; Proffen, T.; Woodward, P. M.; Cheetham, A. K.; Seshadri, R. Local atomic ordering in BaTaO2N studied by neutron pair distribution function analysis and density functional theory. *Chem. Mater.* **2007**, *19*, 4037−4042.

(42) Camp, P. J.; Fuertes, A.; Attfield, J. P. Subextensive entropies and open order in perovskite oxynitrides. *J. Am. Chem. Soc.* **2012**, *134*, 6762−6766.

(43) Niklaus, R.; Minár, J.; Strobel, P.; Schmidt, P. J.; Schnick, W. Ab initio exploration and prediction of AE-containing nitrido(litho/magneso)tetrelates (AE = Ca, Sr; Tt = Si, Ge) with [Si2N6]10- or [Ge2N6]10- units. *Dalton Trans.* **2019**, *48*, 8671−8677.

(44) Xiong, K.; Robertson, J.; Clark, S. J. Passivation of oxygen vacancy states in HfO2 by nitrogen. *J. Appl. Phys.* **2006**, *99*, No. 044105.

(45) Baumgarten, L.; Szyjka, T.; Mittmann, T.; Materano, M.; Matveyev, Y.; Schlueter, C.; Mikolajick, T.; Schroeder, U.; Müller, M. Impact of vacancies and impurities on ferroelectricity in PVD- And ALD-grown HfO2films. *Appl. Phys. Lett.* **2021**, *118*, No. 032903.

(46) Greiner, M. T.; Lu, Z. H. Thin-film metal oxides in organic semiconductor devices: Their electronic structures, work functions and interfaces. *NPG Asia Mater.* **2013**, *5*, No. e55.

(47) Gent, W. E.; Abate, I. I.; Yang, W.; Nazar, L. F.; Chueh, W. C. Design Rules for High-Valent Redox in Intercalation Electrodes. *Joule* **2020**, *4*, 1369−1397.

(48) Yeh, J. J.; Lindau, I. Atomic subshell photoionization cross sections and asymmetry parameters: 1 ≤ Z ≤ 103. *At. Data Nucl. Data Tables* **1985**, *32*, 1−155.

(49) Heymann, L.; Weber, M. L.; Wohlgemuth, M.; Risch, M.; Dittmann, R.; Baeumer, C.; Gunkel, F. Separating the Effects of Band Bending and Covalency in Hybrid Perovskite Oxide Electrocatalyst

Bilayers for Water Electrolysis. *ACS Appl. Mater. Interfaces* **2022**, *14*, 14129−14136.

(50) Schuwalow, S.; Schröter, N. B.; Gukelberger, J.; Thomas, C.; Strocov, V.; Gamble, J.; Chikina, A.; Caputo, M.; Krieger, J.; Gardner, G. C.; Troyer, M.; Aeppli, G.; Manfra, M. J.; Krogstrup, P. Band Structure Extraction at Hybrid Narrow-Gap Semiconductor−Metal Interfaces. *Adv. Sci.* **2021**, *8*, No. 2003087.

(51) Lev, L. L.; Krempaský, J.; Staub, U.; Rogalev, V. A.; Schmitt, T.; Shi, M.; Blaha, P.; Mishchenko, A. S.; Veligzhanin, A. A.; Zubavichus, Y. V.; Tsetlin, M. B.; Volfová, H.; Braun, J.; Minár, J.; Strocov, V. N. Fermi Surface of Three-Dimensional La1-xSrxMnO3 Explored by Soft-X-Ray ARPES: Rhombohedral Lattice Distortion and its Effect on Magnetoresistance. *Phys. Rev. Lett.* **2015**, *114*, No. 237601.

(52) Strocov, V. N.; Wang, X.; Shi, M.; Kobayashi, M.; Krempasky, J.; Hess, C.; Schmitt, T.; Patthey, L. Soft-X-ray ARPES facility at the ADRESS beamline of the SLS: Concepts, technical realisation and scientific applications. *J. Synchrotron Radiat.* **2014**, *21*, 32−44.

(53) Huang, Z.; Wu, Y.; Zhao, Y.; Shi, L.; Huang, R.; Li, F.; Liu, T.; Xu, L.; Gao, H.; Zhou, Y.; Sun, Q.; Ding, S.; Xu, K.; Yang, H. Accurate surface band bending determination on Ga-polar n-type GaN films by fitting x-ray valence band photoemission spectrum. *AIP Adv.* **2019**, *9*, No. 115106.

(54) Cabán-Acevedo, M.; Kaiser, N. S.; English, C. R.; Liang, D.; Thompson, B. J.; Chen, H. E.; Czech, K. J.; Wright, J. C.; Hamers, R. J.; Jin, S. Ionization of high-density deep donor defect states explains the low photovoltage of iron pyrite single crystals. *J. Am. Chem. Soc.* **2014**, *136*, 17163−17179.

(55) Kim, J. K.; Kim, K. J.; Kim, B.; Kim, J. N..; Kwak, J. S.; Park, Y. J..; Lee, J-L.. Effects of surface treatment using aqua regia solution on the change of surface band bending of p-type GaN. *J. Electron. Mater.* **2001**, *30*, 129−133.

(56) Higashi, M.; Yamanaka, Y.; Tomita, O.; Abe, R. Fabrication of cation-doped BaTaO2N photoanodes for efficient photoelectrochemical water splitting under visible light irradiation. *APL Mater.* **2015**, *3*, 2−9.

(57) Hojamberdiev, M.; Vargas, R.; Kadirova, Z. C.; Kato, K.; Sena, H.; Krasnov, A. G.; Yamakata, A.; Teshima, K.; Lerch, M. Unfolding the Role of B Site-Selective Doping of Aliovalent Cations on Enhancing Sacrificial Visible Light-Induced Photocatalytic H2 and O2 Evolution over BaTaO2N. *ACS Catal.* **2022**, *12*, 1403−1414.

(58) Wang, Z.; Luo, Y.; Hisatomi, T.; Vequizo, J. J. M.; Suzuki, S.; Chen, S.; Nakabayashi, M.; Lin, L.; Pan, Z.; Kariya, N.; Yamakata, A.; Shibata, N.; Takata, T.; Teshima, K.; Domen, K. Sequential cocatalyst decoration on BaTaO2N towards highly-active Z-scheme water splitting. *Nat. Commun.* **2021**, *12*, No. 1005.

(59) Gamelin, D. R. Water splitting: Catalyst or spectator? *Nat. Chem.* **2012**, *4*, 965−967.

(60) Hoang, S.; Guo, S.; Mullins, C. B. Coincorporation of N and Ta into TiO2 nanowires for visible light driven photoelectrochemical water oxidation. *J. Phys. Chem. C* **2012**, *116*, 23283−23290.

(61) Marozau, I.; Shkabko, A.; Döbeli, M.; Lippert, T.; Mallepell, M.; Schneider, C. W.; Weidenkaff, A.; Wokaun, A. Pulsed laser deposition and characterisation of perovskite-type LaTiO3-xNx thin films. *Acta Mater.* **2011**, *59*, 7145−7154.

(62) Peter, L. M.; Walker, A. B.; Bein, T.; Hufnagel, A. G.; Kondofersky, I. Interpretation of photocurrent transients at semiconductor electrodes: Effects of band-edge unpinning. *J. Electroanal. Chem.* **2020**, *872*, No. 114234.

(63) Doolittle, L. R. A semiautomatic algorithm for rutherford backscattering analysis. *Nucl. Instrum. Methods Phys. Res., Sect. B* **1986**, *15*, 227−231.

(64) Arstila, K.; Julin, J.; Laitinen, M. I.; Aalto, J.; Konu, T.; Kärkkäinen, S.; Rahkonen, S.; Raunio, M.; Itkonen, J.; Santanen, J. P.; Tuovinen, T.; Sajavaara, T. Potku - New analysis software for heavy ion elastic recoil detection analysis. *Nucl. Instrum. Methods Phys. Res., Sect. B* **2014**, *331*, 34−41.

(65) Strocov, V. N.; Schmitt, T.; Flechsig, U.; Schmidt, T.; Imhof, A.; Chen, Q.; Raabe, J.; Betemps, R.; Zimoch, D.; Krempasky, J.; Wang, X.; Grioni, M.; Piazzalunga, A.; Patthey, L. High-resolution soft X-ray beamline ADRESS at the Swiss Light Source for resonant inelastic X-ray scattering and angle-resolved photoelectron spectroscopies. *J. Synchrotron Radiat.* **2010**, *17*, 631−643.

(66) Ebert, H.; Ködderitzsch, D.; Minár, J. Calculating condensed matter properties using the KKR-Green's function method—recent developments and applications. *Rep. Prog. Phys.* **2011**, *74*, No. 096501.

(67) Tran, F.; Blaha, P. Accurate band gaps of semiconductors and insulators with a semilocal exchange-correlation potential. *Phys. Rev. Lett.* **2009**, *102*, 5−8.

(68) Camargo-Martínez, J. A.; Baquero, R. Performance of the modified Becke-Johnson potential for semiconductors. *Phys. Rev. B* **2012**, *86*, No. 195106.

(69) Hibino, K.; Yashima, M.; Oshima, T.; Fujii, K.; Maeda, K. Structures, electron density and characterization of novel photocatalysts, (BaTaO2N)1-x(SrWO2N)x solid solutions. *Dalton Trans.* **2017**, *46*, 14947−14956.